

Particle orbiting motion in a confined microvortex

Feng Shen

Beijing University of Technology

Zong-He Li

Beijing University of Technology

Ming-Zhu Ai

Beijing University of Technology

Sen Xue

Tsinghua University

Min Xu

Beijing University of Technology

Zhao-Miao Liu (✉ lzm@bjut.edu.cn)

Beijing University of Technology

Research Article

Keywords: Particle orbiting, Slingshot Effect, Particle Motion, Microvortex, Microfluidics.

Posted Date: June 7th, 2021

DOI: <https://doi.org/10.21203/rs.3.rs-598227/v1>

License:   This work is licensed under a Creative Commons Attribution 4.0 International License.

[Read Full License](#)

Particle orbiting motion in a confined microvortex

Feng Shen¹, Zong-He Li¹, Ming-Zhu Ai¹, Sen Xue², Min Xu¹ & Zhao-Miao Liu¹ *

¹ Faculty of Materials and Manufacturing, Beijing University of Technology, Beijing 100124, PR China

² Department of Engineering Mechanics, Tsinghua University, Beijing, 100084, PR China

Correspondence and requests for materials should be addressed to Z-M Liu. (email: lzm@bjut.edu.cn).

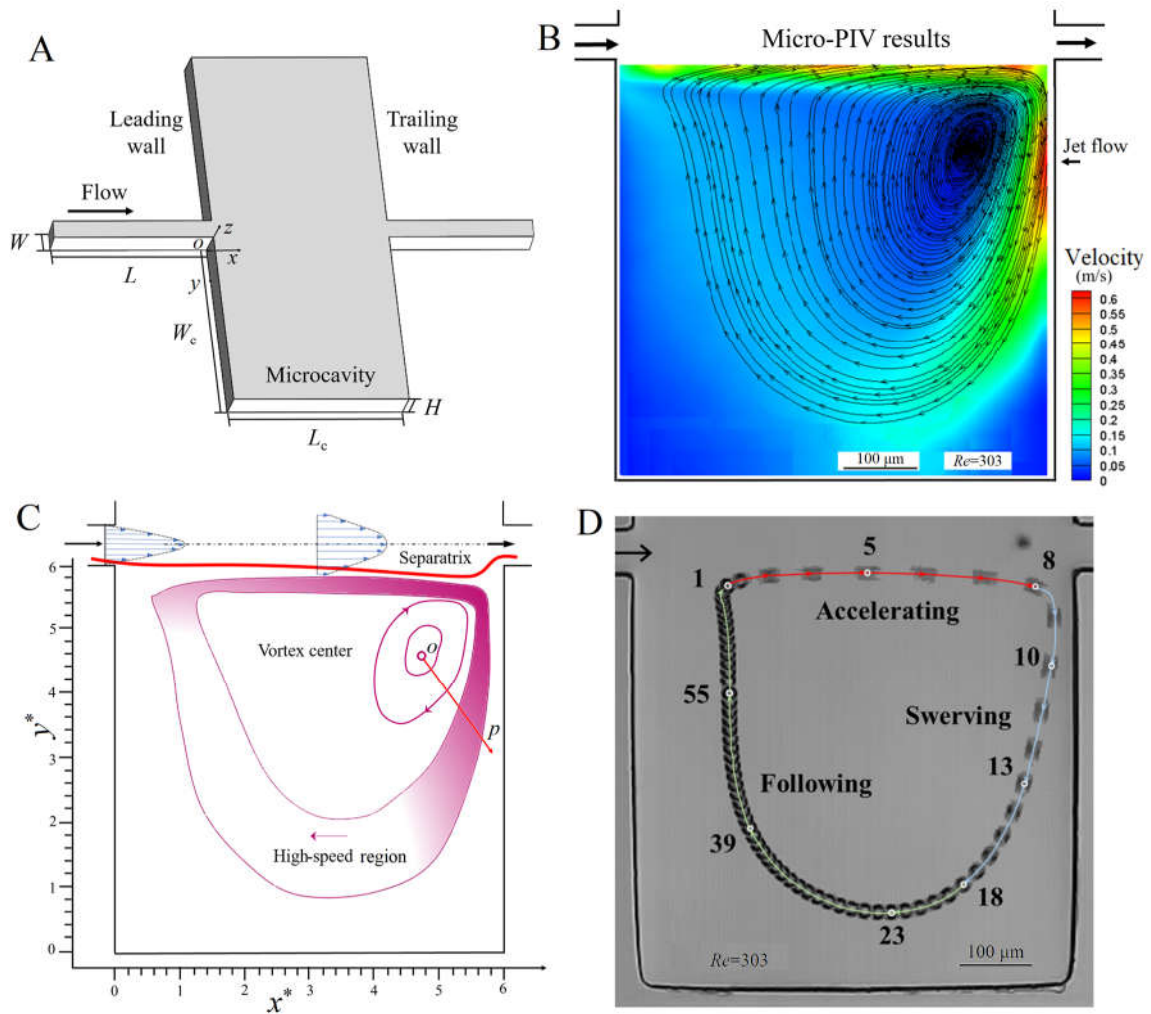
Abstract Particle motion in viscous fluids is a common and fascinating phenomenon. The hydrodynamics of a trapped finite-size particle recirculating along a stable orbit within a microvortex is still puzzling. Herein we report experimental observations of the orbiting motion of a finite-size particle in a vortex confined in a microcavity. The orbiting particle keeps crossing the streamlines with acute changes in velocity along the orbit, which can be divided into three stages: acceleration, swerving, and following. By examining the relationship between particle orbit and vortex streamlines, we uncover a particle slingshot effect and slip motion. Particle motion and vortex structure in three dimensions are also studied, revealing many new fascinating particle motion phenomena. The results provide new insights into the physics of particle motion in vortices.

Key words: Particle orbiting; Slingshot Effect; Particle Motion; Microvortex; Microfluidics.

1 Motion of small beads (particle, droplet, and bubble) in viscous fluids is a common flow phenomenon
2 in nature and is of central importance in many applications ^{1,2}, such as tea leaf paradox ³, particles in
3 physiological flow networks ⁴, spread of viruses via air pollution ⁵, and the manufacturing of multi-core
4 emulsions using microfluidics ⁶. Dating back at least to Stokes ¹, particle motion has always been a focus
5 of research on fluid mechanics ⁷⁻¹⁰, especially recent research on particles/cell manipulations in straight,
6 curved, and spiral microchannels in inertial microfluidics ¹¹⁻¹⁵. Particles exhibit many motions—ordering,
7 focusing, trapping, sorting, clustering, rotating, colliding, and so on ^{16,17}—among which migration across
8 streamlines under the combined effects of inertia and hydrodynamic forces is essential ¹⁶⁻²⁰.

9 Particle orbiting in a laminar vortex confined in a microcavity (or chamber) is one of the most
10 fascinating motions ²¹. In this case, a finite-size particle recirculates along a stable meniscus-shaped orbit
11 without external forces (i.e., no string to supply the needed centripetal force) ^{22,23}. The background
12 physics of interactions between the particle and the vortex is a relatively new area of fluid dynamics and
13 different from those in tubes, parallel shear panels, rotating cylinders, free vortices, and other forms
14 reported in previous studies ²⁴⁻²⁷. The mechanism by which the stable orbit forms relies on a delicate
15 dynamic balance between varying particle forces (centrifugal and inertial forces) and hydrodynamic
16 forces that are locally induced by the flow velocity gradient of the confined vortex ²⁸⁻³¹. As the clam-type
17 vortex structure is three dimensional (3D) and the shape of the particle orbit is neither circular nor
18 elliptical, the acting forces change in a complex way with the location of the particle along the orbit.
19 Moreover, coupled with changes in the velocity of the finite-size particle, these complexities pose a
20 significant challenge to understanding the physics ²⁸⁻³¹. Many issues remain puzzling, especially the
21 relationship between particle trajectory and vortex streamlines, which is crucial for stable maintenance
22 of isolated circulating tumor cells in microcavities for vortex-based microfluidics ³²⁻³⁵.

23 In this work, we provide a deeper understanding of how a finite-size particle recirculates along a stable
24 orbit in a 3D microvortex by comparing the relationship between the particle orbit and the vortex
25 streamlines. Moreover, we also reveal many unique and fascinating particle motions, including deviation
26 from streamlines, change in particle velocity along the orbit, a slingshot effect, slip motion, rotating
27 behaviors, and dancing of bound multi-particles.



28

29 **Figure 1.** Vortex and particle orbit in a microcavity. (A) Schematic of the microfluidic chip with a pair of
 30 rectangular microcavities. (B) Micro-PIV results for the laminar vortex. (C) Separatrix between the vortex
 31 and microchannel flow and the high-speed region of the vortex. The cavity width and length were
 32 nondimensionalized as $x^*=L_c/H$ and $y^*=W_c/H$ ($H=100 \mu\text{m}$). (D) Time-lapse high-speed image of a finite-size
 33 particle ($d=30 \mu\text{m}$) orbiting along a stable meniscus-shaped trajectory in a vortex at a Re of 303 at 6000 fps
 34 (Movie S1).

35

36 Setup and Theoretical Background

37 To compare the relationship between particle orbit and vortex streamlines, we quantitatively measured
 38 the vortex flow velocity vector field in a microcavity ($600 \times 600 \mu\text{m}^2$) using micro-particle image
 39 velocimetry (micro-PIV; Fig. 1A–C). We then visualized the orbiting motion of a finite-size particle
 40 (diameter $d=30 \mu\text{m}$) along a stable meniscus-shaped orbit in the vortex using a high-speed microscopic
 41 imaging system (Fig. 1D). Numerical simulations of the 3D vortex structure were also performed (see
 42 [Materials and Methods](#) for more details).

43 Particle flow in a microchannel can be characterized by the channel Reynolds number $Re = \rho U D_h / \mu$
44 and the particle Reynolds number $Re_p = \rho U_p d / \mu$, where U is the mean velocity of the fluid;
45 $D_h = 2WH / (W + H)$ is the hydraulic diameter of the microchannel (width W and height H); v_p is the
46 characteristic particle velocity; and ρ and μ are the fluid density and dynamic viscosity, respectively³⁰.
47 Fluid velocity in the cavity is substantially less (<10%) than the microchannel flow. The particle velocity
48 v_p changes acutely along the orbit, and Re_p is far below 10^{-3} . As the particle is nearly neutrally buoyant
49 (density ρ_p), the Stokes number $St = (\rho / \rho_p) Re_p \approx Re_p$, which represents the particle inertia³⁰. Flow
50 separation from the leading cavity wall results in the formation of a laminar vortex inside the cavity³⁶.
51 The vortex characteristics (Fig. 1B) are critical for particle trapping and maintenance in the microcavity
52³⁰. In the cavity entrance, flowing target large particles, driven by a shear-gradient lift force scaling with
53 $F_{LS} \sim d^3$, will migrate laterally across the boundary streamlines (separatrix) and enter the vortex region in
54 many complicated ways^{23,29,30,37,38}. Then the isolated particle will recirculate along a stable orbit in a
55 high-speed ring of the vortex region (Fig. 1C). Here we focus mainly on the particle orbiting behavior
56 to reveal the background physics.

57 The motion of a rigid, spherical particle of radius a in a dilute suspension can be described by a form
58 of Newton's Second Law delineated by Maxey and Riley^{30,39},

$$59 \quad m_p \frac{dV_p}{dt} = m_f \frac{D\mathbf{u}}{Dt} \Big|_{\mathbf{Y}(t)} - \frac{1}{2} m_f \frac{d}{dt} \left(V_p(t) - \mathbf{u}[\mathbf{Y}(t), t] - \frac{1}{10} a^2 \nabla^2 \mathbf{u} \Big|_{\mathbf{Y}(t)} \right) + (m_p - m_f) \mathbf{g} - 6\pi a \mu \left(V_p(t) - \mathbf{u}[\mathbf{Y}(t), t] - \frac{1}{6} a^2 \nabla^2 \mathbf{u} \Big|_{\mathbf{Y}(t)} \right)$$

60 where m_p is the mass of the particle, m_f is the mass of the fluid displaced by the particle, V_p is the center-
61 of-mass velocity of the particle located at $\mathbf{Y}(t)$ at time t , \mathbf{u} is the undisturbed fluid velocity, and \mathbf{g} is the
62 gravitational acceleration. The terms on the right-hand side of this equation are, from left to right, the
63 pressure gradient force, the added mass force, the gravitational body force, and the Stokes drag force.
64 The contributions of inertia are implicitly stated by this equation. This equation has been explained in
65 further detail in previous studies^{29,30}. It has been widely used to model particle transport^{40,41} and can
66 generally describe the main forces exerted on the orbiting particle in a microvortex; however, as it is
67 based on creeping flow, it does not include other weaker forces, such as the Saffman lift related to the
68 velocity shear or wall effects or the Basset history force for particles with changes in velocity, which will

69 induce novel particle motions in three dimensions observed in our experiments. Moreover, the effects of
70 the microcavity walls are not considered by this equation, and the fluid velocity field of the vortex is in
71 three dimensions, which should be known at the outset.

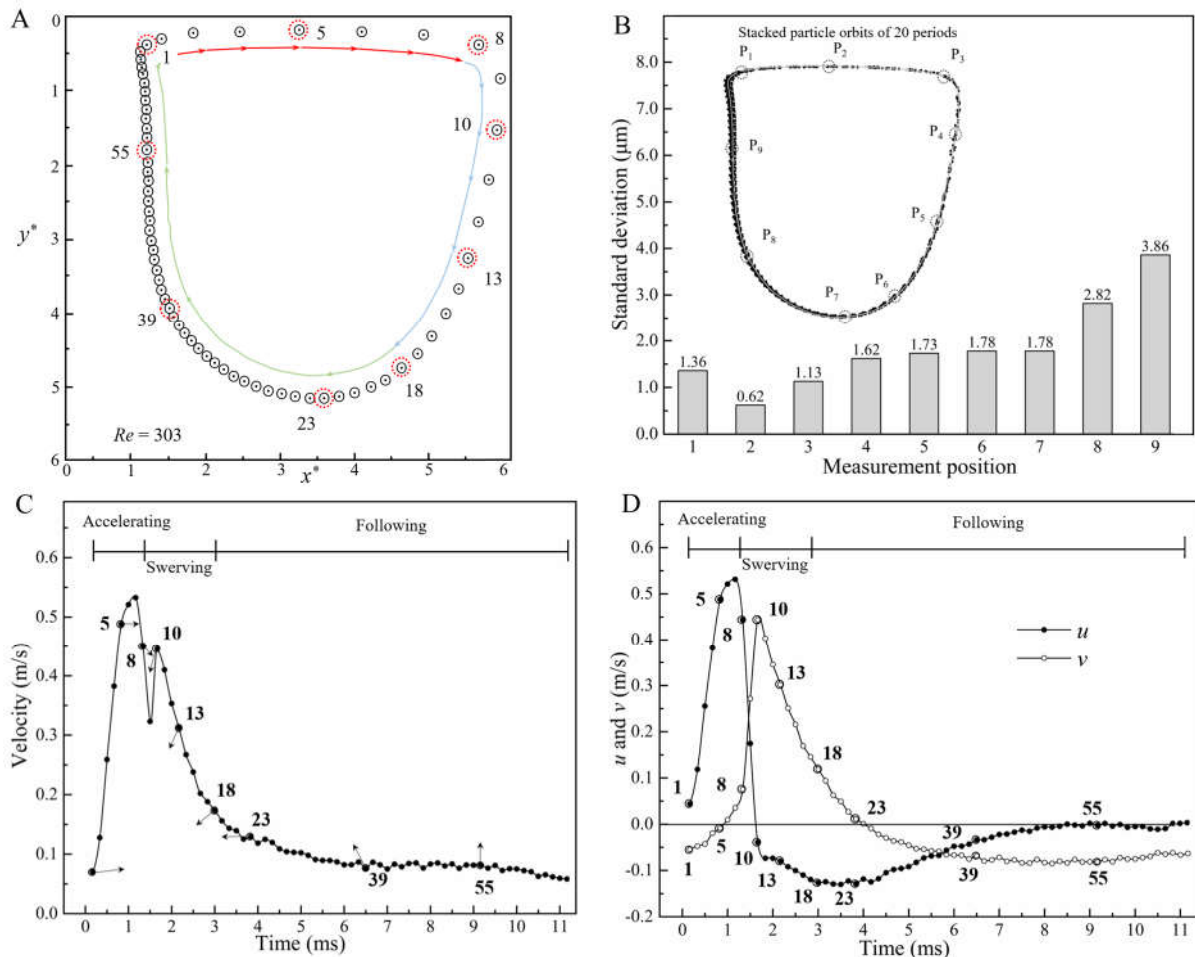
72 In a naive view, the particle is following the streamlines and the exerting forces are balanced. In fact,
73 the finite-size particle keeps migrating across the streamlines and the forces cannot be in equilibrium.
74 The odd particle orbit results from the combined effects of inertia and hydrodynamic forces. In fact, the
75 real problem is much more complex, with three features^{23,28-30}: (i) the particle velocity is spatially and
76 temporally variable, not constant throughout the orbit, which should be characterized quantitatively; (ii)
77 the meniscus-shaped orbit is not circular; and (iii) the velocity profile of the vortex is clam-type in three
78 dimensions, which increases the complexity of the shear gradient. Both inertia and wall effects can
79 substantially influence the motion of particles inside the cavity. Inertia causes the particle to cross the
80 vortex streamlines, and all other effects result in acceleration and deceleration of the particle along the
81 orbit. As particle orbiting behavior is the result of the multiple aforementioned factors, it is not possible
82 to quantitatively explain the individual effects of each factor. To date, several physical aspects remain
83 open questions.

84 **Results**

85 **Particle orbit and velocity change.** To quantitatively reveal the particle dynamics, we processed the
86 recorded particle images and extracted the particle velocities along the orbit. Figure 2A and Movie S1
87 show that the particle can recirculate periodically along a meniscus-shaped odd orbit. In one period
88 (about 11 ms), 67 particle images were recorded at 6000 frames per second (fps). To accurately depict
89 the morphology of the orbit, we stacked the particle images from a single period. Based on the particle
90 velocity and locations, the orbit can be divided into three stages: accelerating (nos. 1–8), swerving (nos.
91 9–18), and following (nos. 19–67). Deviation of the particle from the orbit at nine positions over 20
92 periods was also measured (Fig. 2B). The maximum value is 3.86 μm ($<30 \mu\text{m}$), which proves that the
93 particle orbit is stable. An interesting question is how can the particle recirculate along the stable odd
94 orbit without a string to supply the centripetal force in the vortex.

95 In the accelerating stage (Fig. 2C), the magnitude of the particle velocity (v_p) increases from 0.06 to

96 0.54 m/s driven by the flow shear effect of the microchannel flow. In the swerving stage, the v_p decreases
 97 rapidly. At 1.5 ms, the particle begins to swerve to the y -direction as the effect of the trailing cavity wall
 98 and the v_p decrease to a low value of 0.32 m/s. In the following stage, the mean v_p of 0.0896 m/s is much
 99 smaller than that of the microchannel flow ($U=4.04$ m/s). The change in x -velocity (u) and y -velocity (v)
 100 was also determined (Fig. 2D). In the accelerating stage, u increases rapidly under high acceleration. In
 101 the swerving stage, u decreases rapidly while v increases and then decreases quickly. The change in
 102 particle velocity along an orbit is a result of the combined effects of particle–vortex interactions and the
 103 confined effects of the cavity walls. The change in particle velocity found here agrees with that in a
 104 previous study³⁰; however, our results are more systematic and detailed and therefore are useful for
 105 further theoretical analyses of forces.

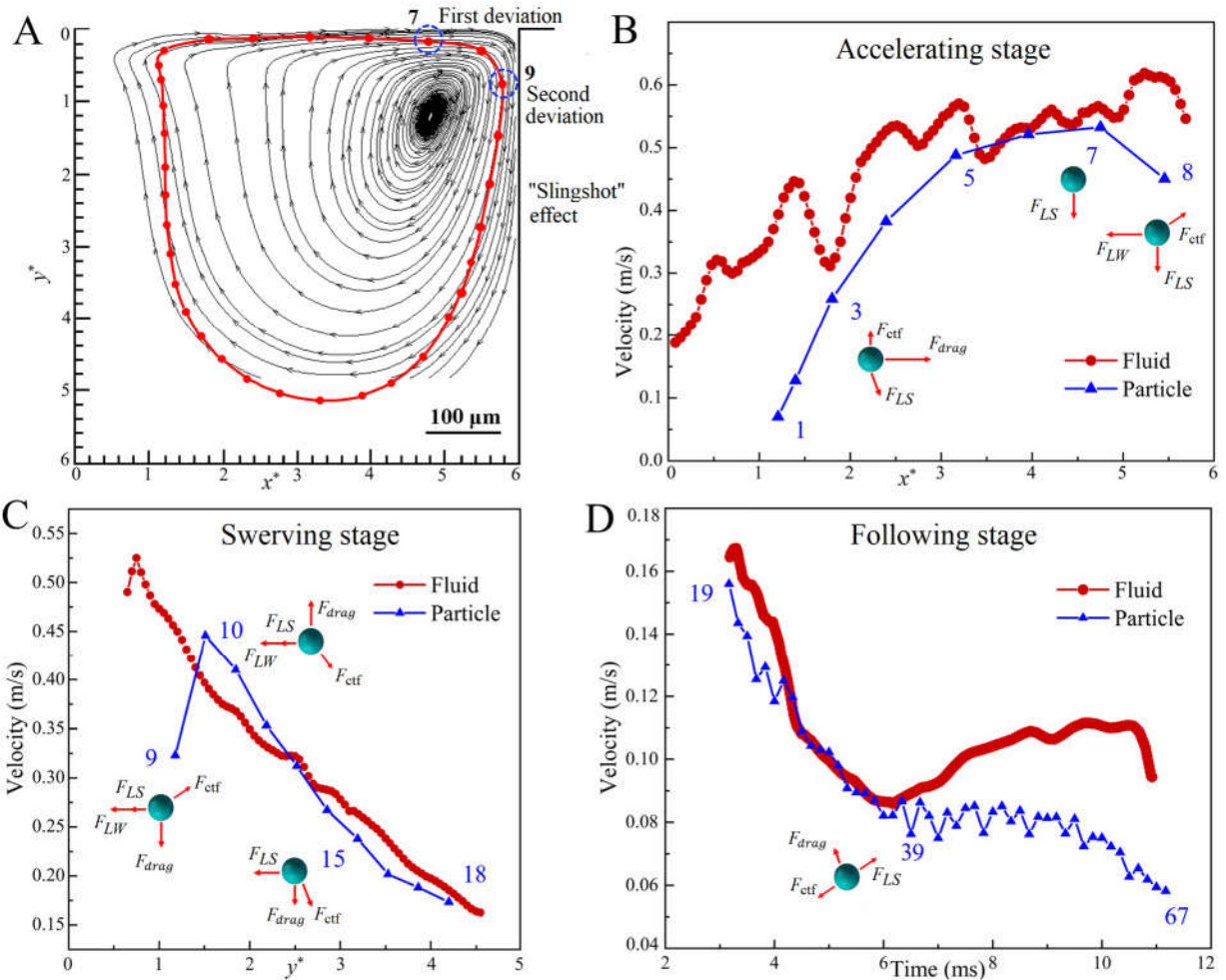


106
 107 **Figure 2.** Changes in particle orbit and velocity. (A) Particle numbers along an orbit at $Re=303$. The
 108 accelerating stage is nos. 1–8, the swerving stage is nos. 9–18, and the following stage is nos. 19–67. (B)
 109 Deviation in particle location over 20 periods. (C) Change of the particle velocity along an orbit (the arrows
 110 show the direction of the velocity). (D) x -velocity (u) and y -velocity (v) at different locations.

111
112
113
114
115
116
117
118
119
120
121
122
123
124
125
126
127
128
129
130
131
132
133
134
135
136

The relationship between particle orbit and vortex streamlines. Small tracer particles ($<1 \mu\text{m}$) tend to follow the surrounding fluid flow, whereas finite-size particles with a diameter comparable to the microchannel size will deviate from the streamlines. Therefore, the particle trajectory is different from the surrounding streamlines, especially in flow fields with fluid velocity acceleration and deceleration or in curved streamlines. The deviation between them is the essence of particle dynamics and critical to revealing the background physics¹⁶⁻²⁰. Although many studies have suggested that the finite-size particle will deviate from the curved streamlines^{29,30}, to the best of our knowledge this has not been observed directly in experiments. In this study, for the first time, we identified the deviation between the particle trajectory and vortex streamlines (Fig. 3A) by comparing results from a micro-PIV system and a high-speed microscopic imaging system. Figure 3 shows that the orbiting finite-size particle keeps on crossing the streamlines, inducing morphological deviation and velocity mismatching between itself and the surrounding fluid.

Particle (nos. 1–6) first follows the streamlines (Fig. 3A). Both the particle and the surrounding fluid rapidly accelerate their u -velocities, but the particle lags behind the fluid, as its velocity is lower than the fluid velocity (Fig. 3B). The fluid in the separatrix region is accelerated by the shear effects of the microchannel flow, whereas the particle is accelerated mainly by the flow drag force $F_{drag} = 3\pi\mu d v_t (1 + 0.15 Re_p^{0.687})$ ¹¹, where $v_t = v_f - v_p$ is the difference between the fluid velocity v_f and the particle velocity v_p . The estimated mean F_{drag} and particle acceleration in this stage are about $1.54 \times 10^{-7} \text{ N}$ and 129.6 m/s^2 , respectively. Then, in front of the trailing wall (no. 7, $x^* \sim 4$ and $t = 0.98 \text{ ms}$), the particle first deviates from the streamlines laterally inward toward the vortex center, which is induced by the fluid shear-gradient force $F_{LS} \propto \rho U d^3 \dot{\gamma}$ ^{30,34}. Particle no. 7 is accelerated to the maximum u -velocity of 0.54 m/s and F_{LS} becomes dominant, which causes the particle's v -velocity to begin to increase. Please note that the existing centrifugal force $F_{cf} = \pi d^3 (\rho_p - \rho) v_p^2 / 6r$, where r is the local radius of the particle trajectory curvature, acts in an opposing outward direction from the vortex center to the particle ($o-p$) and also increases near the trailing wall²³.



137
 138 **Figure 3.** The relationship between the vortex streamlines and particle orbit. (A) Deviation in morphological
 139 characteristics. (B) Particle acceleration in the x -direction and deviation in the y -direction in stage I. (C)
 140 Particle swerving near the trailing wall and the slingshot effect in stage II. (D) Particle following of the
 141 streamlines in stage III at low speeds.

142
 143 Particle no. 9 begins its second deviation toward the y -direction under the influence of many complex
 144 effects. The first effect is the trailing wall-induced force $F_{LW} \propto \rho U^2 d^6 / H_w^4$, which increases
 145 significantly with the decrease in distance (H_w) between the particle and the trailing wall^{30,34}. The second
 146 effect is the stagnation flow area near the trailing wall predicted in our previous study^{37,38}, which causes
 147 the u -velocity to decrease dramatically to zero for particle nos. 7–9 (Fig. 2D). The third effect is the high-
 148 speed jet flow (Fig. 1B), which results from the separated fluid of the separatrix. The jet flow dominates
 149 the particle's second deviation toward the y -direction and accelerates its v -velocity from no. 9 to no. 10
 150 (Fig. 2D), causing the increase in velocity of particle no. 10 (Fig. 3C). Furthermore, the fluid velocity at
 151 no. 9 is higher than that of the particle, which means that it is easier for the fluid to swerve.

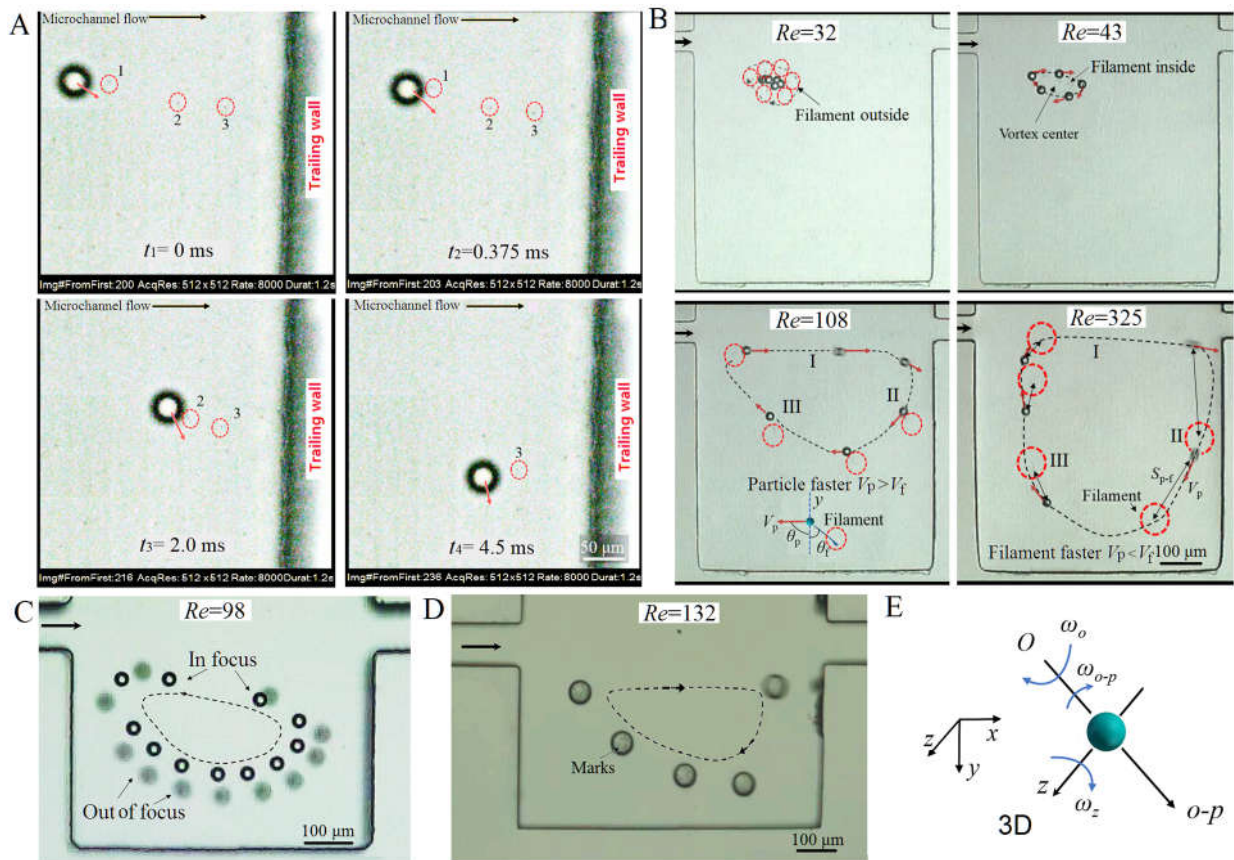
152 Then, for particle nos. 10–18, the particle and fluid decrease their speeds as y^* increases. The particle
153 keeps crossing the curved streamlines (Fig. 3C), a slingshot effect induced by particle inertia. This
154 phenomenon occurs in many flow fluids with curved streamlines. In the following stage, particle nos.
155 19–67 have good following performance with very low velocity magnitudes, and the elapsed time is
156 relatively long (about 9 ms). Therefore, the hydrodynamic forces exerted on the particle are relatively
157 smaller. During an orbit, in the $o-p$ direction, the component F_{LS} is always opposite F_{cf} . As a result
158 of changes in particle velocity in a non-uniform vortical flow field, the direction and magnitude of the
159 forces change acutely along an orbit. The mechanistic description of these forces is lacking and
160 challenging³⁰. Moreover, other weaker forces (e.g., the Saffman lift and the Basset history force) have
161 not been considered. Please note that because of the short particle orbit and the low frequency of the
162 micro-PIV system (<15 Hz), the finite-size particle was absent in the micro-PIV experiments.

163

164 **Fascinating 3D particle motions.** Both the particle motion and the fluid flow are in three dimensions.
165 Here, to reveal the difference in their dynamics, we visualized their 3D motions simultaneously using a
166 high-speed microscopic imaging system. Figure 4A shows that the finite-size particle ($d=30\ \mu\text{m}$) catches
167 up with the tracers out front ($d=0.86\ \mu\text{m}$) during the swerving stage near the trailing wall in cavity II
168 ($L_c=600\ \mu\text{m}$, $W_c=400\ \mu\text{m}$, and $H=200\ \mu\text{m}$). It seems as if the particle slips through the surrounding fluid
169 at a higher velocity. To the best of our knowledge, this is the first time this fascinating slip motion, which
170 is a result of particle size and density, the cavity walls, and 3D characteristics of the vortex, has been
171 observed in a microvortex. Moreover, careful observation of Movie S2 shows that the tracers disappear
172 a few times after traveling a short distance, which indicates that they have a small z -direction velocity
173 (w) and are moving out of the focus plane ($\sim 50\ \mu\text{m}$) in three dimensions.

174 Interestingly, we also observed two contradictory phenomena (Fig. 4B and Movie S3). In our
175 experiments, the particle is accidentally enwound by a thin filament (like a tail). At $Re=32$, the finite-
176 size particle is orbiting near the vortex core and a small tail moves outside of its track. In contrast, at
177 $Re=43$, the particle track expands and the tail migrates to the inside of the particle track. Another
178 paradoxical phenomenon at $Re=108$ and 325 is more fascinating. At a moderate Re of 108, both the

179 particle and the tail move at the same velocity in stage I, whereas the particle moves faster than the
 180 following tail in stages II and III ($V_p > V_f$). The angles between the y axis and particle velocity vector (θ_p)
 181 and the tail direction (θ_f) change at different locations along the orbit. In contrast, at $Re=325$, the tail is
 182 always ahead of the accompanying particle. The distance (S_{p-f}) between them increases in stages I and
 183 II, which indicates that the tail velocity is higher than the particle velocity ($V_p < V_f$). Please note that the
 184 tail with low density has become elongated at $Re=108$ and 325 . These intriguing phenomena were
 185 observed for the first time in our experiments.

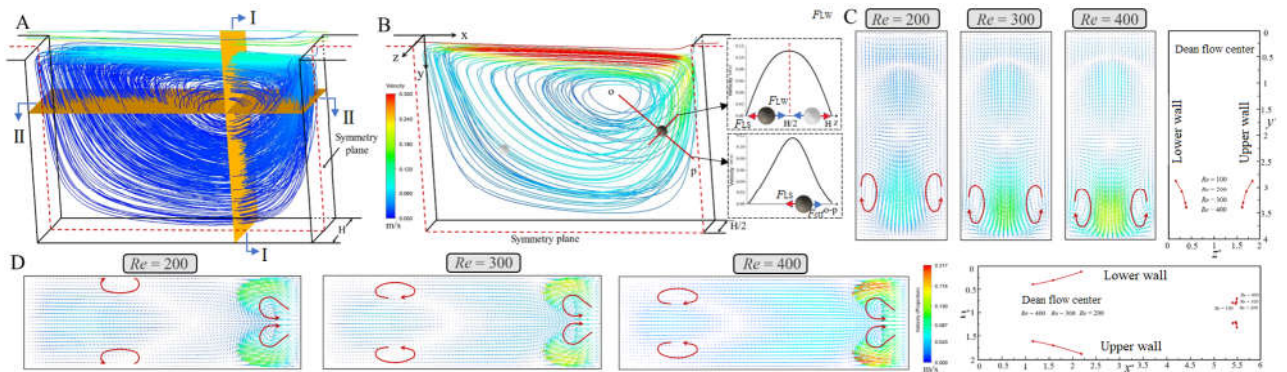


186
 187 **Figure 4.** Observations of intriguing three-dimensional particle motions. (A) Local magnification of slip
 188 motion, in which a $d=30 \mu\text{m}$ particle catches up to three tracers out front ($d=0.86 \mu\text{m}$) in 4.5 ms during the
 189 swerving stage (Movie S2). The tracers disappear a few times after traveling a small distance. (B) Two
 190 paradoxical moving phenomena of particles and accompanying filaments (tails) at different Reynolds
 191 numbers (Movie S3). (C) Stacked particle images showing two simultaneous particle orbits in two parallel z -
 192 planes in microcavity II. The white particle is in the focus plane, whereas the gray particle is out of the focus
 193 plane (Movie S4). (D) 3D rotation of a big oil bead ($d=50 \mu\text{m}$) with spots as marks (Movie S5). (E) Schematic
 194 illustration of particle 3D rotation (ω_o , ω_z , and ω_{o-p}).

195
 196

197 The reasons for these phenomena (Fig. 4A and B) are very complex and partly related to the 3D vortex
 198 structure. We speculate that the z -plane of the tracer and tail may differ from that of the finite-size particle.
 199 When they are traveling in the middle z -plane their speed is high, whereas near the upper or lower cavity
 200 walls it is relatively low. The tracer and tail have better following performance and can easily change
 201 their z -plane in the 3D flow field. In contrast, the finite-size particle always keeps a distance from the
 202 walls because of F_{LW} , which repels it. Therefore, their velocities are different. Furthermore, we observed
 203 two finite-size particles simultaneously recirculating in two orbits in two parallel x - y planes (Fig. 4C and
 204 Movie S4). The white particle is in the focus plane, whereas the gray particle is outside the focus plane.
 205 A previous study also predicted that the particle may have two orbital planes in the z -direction (38). The
 206 orbital plane position in the z -direction is determined by the balance of F_{LS} acting towards the upper or
 207 lower walls with the opposite F_{LW} . The tracers and tail are more easily affected by the surrounding fluid,
 208 resulting in different moving behaviors.

209 Moreover, we observed 3D rotating behaviors of an orbiting oil bead ($d=50\ \mu\text{m}$) with spots as marks
 210 (Fig. 4D and Movie S5). In addition to rotating clockwise (ω_o), the bead rotates around the z axis (ω_z),
 211 which is caused by the velocity gradient along the o - p axis. We previously observed particle ω_z rotation
 212 ⁴²; however, in this study the bead also shows a more complex rotation around the o - p axis (ω_{o-p})
 213 simultaneously. The 3D rotation is due to the non-uniform velocity gradients across the bead (Fig. 4E).



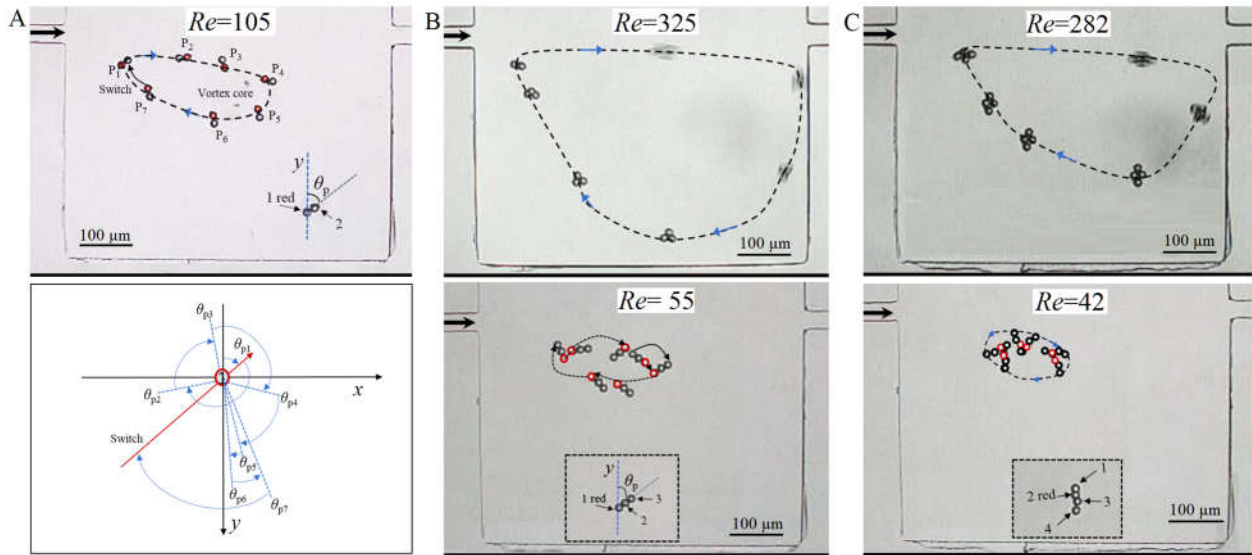
214
 215 **Figure 5.** Numerical simulation of the 3D vortex structure confined in microcavity II at different Reynolds
 216 numbers. (A) Streamlines of the vortex with the horizontal and vertical cross-sections passing through the
 217 vortex center. (B) Cross-section of the 3D vortex structure and illustrations of non-uniform fluid velocity
 218 gradients across the particle along the o - p and z -directions. (C) Flow velocity vector fields on the I-I cross-
 219 section to visualize Dean flow (two symmetrical counter-rotating vortices). (D) Flow velocity vector fields
 220 on the II-II cross-section showing Dean flow. The center of the Dean flow evolves as the Re increases from
 221 100 to 400. The velocities in different horizontal planes at a Re of 300 are shown in Fig. S1.

222 **Vortex 3D structure.** To reveal the background physics, we simulated the 3D vortex structure (Fig. 5A),
223 which is clam shaped and symmetrical about the z -plane at $z=0.5H$. The simulated result shows that the
224 vortex is 3D, which is consistent with the simulation of Zhou et al. (2013). The velocity distributions
225 along the $o-p$ direction and z -direction across the particle are non-uniform (Fig. 5B), which induces the
226 particle 3D rotation. The velocities in different horizontal planes at a $Re=300$ are shown in Fig. S1.

227 Interestingly, we also found Dean secondary flow in the 3D vortex field (Fig. 5C and D). As Re
228 increases from 110 to 532, the center of the Dean flow moves toward the sidewall and the leading wall,
229 dragging the particle outward along the $o-p$ direction. Dean flow has also been used to explain particle
230 migrations in curved or spiral microchannels^{11,12} and the tea leaf paradox³, in which the leaves
231 accumulate in the center of a cup. To the best of our knowledge, this is the first time that Dean flow has
232 been found in a microvortex confined in a cavity. The vortex center can be regarded as a wall, forming
233 a curved channel with the other walls. The effects of Dean flow on the tracers and tails are more
234 significant than its effects on the finite-size particle, which leads to the w -velocity of the tracers.

235
236 **Dancing of bound multi-particles.** We also observed many unexpected but amazing flow phenomena
237 among two-, three-, and four-bound multi-particles (Fig. 6 and Movies S6–S8), which seem to be
238 dancing in the vortices. The two-bound multi-particle rotates 270° around the no. 1 particle for one orbit
239 and then switches no. 1 to no. 2 (Fig. 6A). The trilobal multi-particle moves faster in stages I and II and
240 rotates violently, whereas the three-linear-type multi-particle rotates and somersaults during orbiting (Fig.
241 6B). The four-arrays-type multi-particle rotates and recirculates simultaneously, which makes it look like
242 it is dancing a graceful waltz. The four-linear-type multi-particle dances a dance of four little swans
243 around the vortex center (Fig. 6C). The background physics of these flow phenomena are very complex
244 and have not been addressed. To the best of our knowledge, these fascinating multi-particle flow
245 phenomena, which can enrich the knowledge of particle motion in vortices, were observed for the first
246 time in our experiments.

247



248
 249 **Figure 6.** 3D dancing motions of bound multi-particles in microcavity II. (A) Two-bound multi-particle
 250 rotation during orbiting (Movie S6). Particle no. 1 is marked in red. (B) Orbiting of trilobal multi-particles
 251 (upper) and three-linear-type multi-particles (lower) around the vortex center (Movie S7). (C) Dancing
 252 motions of four-arrays-type multi-particles (upper) and four-linear-type multi-particles (lower; Movie S8).
 253 Particle no. 2 is marked in red.

254
 255 **Discussion**

256 We have quantitatively measured the changes in particle velocity during orbiting and the deviation of
 257 the particle trajectory from the vortex streamlines, which are useful for further theoretical analysis of
 258 forces. The particle orbit can be divided into three stages: accelerating, swerving, and following. The
 259 effects of inertia and hydrodynamic forces at each stage have been analyzed as well. The phenomena of
 260 the particle slingshot effect, slip motion, and 3D rotation (ω_o , ω_z , and ω_{o-p}) are fascinating and deepen
 261 understanding of the background physics. To the best of our knowledge, and despite the general
 262 consensus that particles migrate across streamlines as a result of particle–vortex interactions, there are
 263 no previous reports in the literature of such detailed observations of the 3D orbiting and rotating motions
 264 of a finite-size particle as documented in this paper. Moreover, the 3D vortex structure and multi-particle
 265 3D orbiting phenomena demonstrated here are unique and indicate complex physics. The results provide
 266 new insights into the dynamics of particle motion in vortices.

267 **Materials and Methods**

268 The fabricated polydimethylsiloxane (PDMS) microfluidic chips ($2.5 \times 4.5 \text{ cm}^2$) consisted of a straight
 269 microchannel ($W=60 \text{ }\mu\text{m}$) with a pair of rectangular microcavities located symmetrically on both sides

270 (Fig. 1A). Microcavity I ($L_c=W_c=600\ \mu\text{m}$ and $H=100\ \mu\text{m}$) was used for two-dimensional observation,
271 whereas microcavity II ($L_c=600\ \mu\text{m}$, $W_c=400\ \mu\text{m}$, and $H=200\ \mu\text{m}$) was used for 3D observation. Polymer
272 microspheres (density $\rho_p=1.03\ \text{g/cm}^3$, average diameter $d=30\ \mu\text{m}$, Duke standards; Fremont, CA, USA)
273 suspended in deionized water ($\rho=1.0\ \text{g/cm}^3$ and $\mu=10^{-3}\ \text{Pa}\cdot\text{s}$) were used as the finite-size particles. We
274 set the particle concentration to about 1–2 particles per 10 mL to avoid particle–particle interactions.
275 Once a single particle was trapped, injection of the particle suspension was stopped and deionized water
276 was injected from another inlet at a fixed flow rate of 0.15–1.56 mL/min with a syringe pump (PHD2000,
277 Harvard Apparatus; Holliston, MA, USA) with corresponding Reynolds numbers of 32–325.

278 To compare the relationship between particle orbit and vortex streamlines, we quantitatively measured
279 the vortex flow velocity vector field in the microcavity ($600\times 600\ \mu\text{m}^2$) using micro-particle image
280 velocimetry (micro-PIV, Dantec Dynamics, Skovlunde Denmark; Fig. 1B and C). Polystyrene beads
281 (average diameter= $0.86\ \mu\text{m}$, density= $1.05\ \text{g/cm}^3$; Thermo Fisher) were used as tracers to visualize the
282 vortex flow. Details of the micro-PIV system were described previously³⁶. We then visualized the
283 orbiting motion of a finite-size particle (diameter $d=30\ \mu\text{m}$) along a stable meniscus-shaped orbit in the
284 vortex using a high-speed microscopic imaging system (Fig. 1D), consisting of an inverted microscope
285 (IX73, Olympus; Japan) and a high-speed digital video camera (Phantom v7.3; Vision Research Inc.,
286 Wayne, NJ, USA) with a frame rate of up to 30,000 fps. The captured images were resampled and
287 analyzed with MATLAB to identify the particle center and to calculate its velocities at different locations
288 along the orbit. Tracer flows accompanying the finite-size particle were recorded to visualize and
289 compare their real trajectory in three dimensions. We simulated the 3D vortex structure using a finite-
290 volume Navier-Stokes solver on structured meshes. ANSYS-Fluent (v17.0) was used as the simulation
291 software with appropriate, second-order accurate, discretization schemes in space and time.

292 **References**

- 293 1. Leal, L.G. Particle motions in a viscous fluid. *Annu Rev Fluid Mech* **12**, 435-476(1980).
- 294 2. D'Avino, G., Greco, F. & Maffettone, P.L. Particle migration due to viscoelasticity of the suspending liquid
295 and its relevance in microfluidic devices. *Annu Rev Fluid Mech* **49(1)**, 341-360 (2017).
- 296 3. Amit, T. & John, M. Einstein's tea leaves and pressure systems in the atmosphere. *The Physics Teacher* **48**,
297 292-295 (2010).
- 298 4. Vigolo, D., Radl, S. & Stone, H.A. Unexpected trapping of particles at a T junction. *PNAS* **111(13)**, 4770-
299 4775 (2014).

- 300 5. Comunian, S., Dongo, D., Milani, C. & Palestini, P. Air pollution and COVID-19: the role of particulate
301 matter in the spread and increase of COVID-19's morbidity and mortality. *Int J Environ Res Public Health*
302 **17(12)**, 4487 (2020).
- 303 6. Tiribocchi, A., Montessori, A., Lauricella, M., Bonaccorso, F., Succi, S., Aime, S., Milani, M. & Weitz, D.A.
304 The vortex-driven dynamics of droplets within droplets. *Nature Communications* **12**, 1-10 (2021).
- 305 7. Angilella, J.-R., Vilela, R.D. & Motter, A.E. Inertial particle trapping in an open vortical flow. *J Fluid Mech*
306 **744**, 183-216 (2014).
- 307 8. Hood, K., Lee, S. & Roper, M. Inertial migration of a rigid sphere in three-dimensional Poiseuille flow. *J*
308 *Fluid Mech* **765**, 452-479 (2015).
- 309 9. Asmolov, E.S., Dubov, A.L., Nizkaya, T.V., Harting, J. & Vinogradova, O.I. Inertial focusing of finite-size
310 particles in microchannels. *J Fluid Mech* **840**, 613-630 (2018).
- 311 10. Morita, Y., Itano, T. & Sugihara-Seki, M. Equilibrium radial positions of neutrally buoyant spherical particles
312 over the circular cross-section in Poiseuille flow. *J Fluid Mech* **813**, 750-767 (2017).
- 313 11. Zhang, J., Yan, S., Yuan, D., Alici, G., Nguyen, N.-T., Warkiani, M.E. & Li, W. Fundamentals and
314 applications of inertial microfluidics: a review. *Lab Chip* **16(1)**, 10-34 (2016).
- 315 12. Stoecklein, D. & Di Carlo, D. Nonlinear Microfluidics. *Anal Chem* **91**, 296-314 (2019).
- 316 13. Luan, Q., Macaraniag, C., Zhou, J. & Papautsky, I. Microfluidic systems for hydrodynamic trapping of cells
317 and clusters. *Biomicrofluidics* **14**, 031502 (2020).
- 318 14. Volpe, A., Gaudioso, C. & Ancona, C. Sorting of particles using inertial focusing and laminar vortex
319 technology: a review. *Micromachines* **10**, 594 (2019).
- 320 15. Nasiri, R., Shamloo, A., Ahadian, S., Amirifar, L., et al. Microfluidic-based approaches in targeted
321 cell/particle separation based on physical properties, fundamentals and applications. *Small* 2000171 (2020).
- 322 16. Di Carlo, D., Edd, J.F., Humphry, K.J., Stone, H.A. & Toner, M. Particle segregation and dynamics in
323 confined flows. *Phys Rev Lett* **102(9)**, 094503 (2009).
- 324 17. Stan, C.A., Ellerbee, A.K., Guglielmini, L., Stone, H.A. & Whitesides, G.M. The magnitude of lift forces
325 acting on drops and bubbles in liquids flowing inside microchannels. *Lab Chip* **13**, 365-376 (2013).
- 326 18. Mutlu, B.R., Edd, J.F. & Toner, M. Oscillatory inertial focusing in infinite microchannels. *PNAS*, **115(30)**,
327 7682-7687 (2018).
- 328 19. Li, Q., Abbas, M., Morris, J.F., Climent, E. & Magnaudet, J. Near-wall dynamics of a neutrally buoyant
329 spherical particle in an axisymmetric stagnation point flow. *J Fluid Mech* **892**, A32 (2020).
- 330 20. Haddadi, H., Shojaei-Zadeh, S., Connington, K. & Morris, J.F. Suspension flow past a cylinder, particle
331 interactions with recirculating wakes. *J Fluid Mech* **760**, R2 (2014).
- 332 21. Shelby, J.P., Lim, D.S.W., Kuo, J.S. & Chiu, D.T. High radial acceleration in microvortices. *Nature* **425**, 38
333 (2003).
- 334 22. Raihan, M.K., Li, D., Kummetz, A.J., Song, L., Yu, L.D. & Xuan, X.C. Vortex trapping and separation of
335 particles in shear thinning fluids. *Appl Phys Lett* **116**, 183701 (2020).
- 336 23. Mach, A.J., Kim, J.H., Arshi, A., Hur, S.C. & Di Carlo, D. Automated cellular sample preparation using a
337 centrifuge-on-a-chip. *Lab Chip* **11**, 2827-2834 (2011).
- 338 24. Sauma-Pérez, T., Johnson, C.G., Yang, L., Mullin, T. An experimental study of the motion of a light sphere
339 in a rotating viscous fluid. *J Fluid Mech* **847**, 119-133 (2018).
- 340 25. Candelier, F., Mehlig, B. & Magnaudet, J. Time-dependent lift and drag on a rigid body in a viscous steady
341 linear flow. *J Fluid Mech* **864**, 554-595 (2019).
- 342 26. Shi, P., Rzehak, R., Lucas, D. & Magnaudet, J. Hydrodynamic forces on a clean spherical bubble translating
343 in a wall-bounded linear shear flow. *Phys Rev Fluids* **5**, 073601 (2020).

- 344 27. Kurose, R. & Komori, S. Drag and lift forces on a rotating sphere in a linear shear flow. *J Fluid Mech* **384**,
345 183-206 (1999).
- 346 28. Lim, D.S.W., Shelby, J.P., Kuo, J.S. & Chiu, D.T. Dynamic formation of ring-shaped patterns of colloidal
347 particles in microfluidic systems. *Appl Phys Lett* **83**, 1145 (2003).
- 348 29. Haddadi, H., Naghsh-Nilchi, H. & Di Carlo, D. Separation of cancer cells using vortical microfluidic flows.
349 *Biomicrofluidics* **12**, 014112 (2018).
- 350 30. Haddadi, H. & Di Carlo, D. Inertial flow of a dilute suspension over cavities in a microchannel. *J Fluid Mech*
351 **811**, 436-467 (2017).
- 352 31. Jiang, M., Qian, S. & Liu, Z. Fully resolved simulation of single-particle dynamics in a microcavity.
353 *Microfluid Nanofluid* **22**, 144 (2018).
- 354 32. Dhar, M., Lam, J.N., Walser, T., Dubinett, S.M., Retting, M.B. & Di Carlo, D. Functional profiling of
355 circulating tumor cells with an integrated vortex capture and single-cell protease activity assay. *PNAS* **115(40)**,
356 9986-9991 (2018).
- 357 33. Zhou, J., Kasper, S. & Papautsky, I. Enhanced size-dependent trapping of particles using microvortices.
358 *Microfluid Nanofluid* **15**, 611-623 (2013).
- 359 34. Wang, X., Yang, X. & Papautsky, I. An integrated inertial microfluidic vortex sorter for tunable sorting and
360 purification of cells. *Technology* **4**, 88-97 (2016).
- 361 35. Khojah, R., Stoutamore, R. & Di Carlo, D. Size-tunable microvortex capture of rare cells. *Lab Chip* **17**, 2542-
362 2549 (2017).
- 363 36. Shen, F., Xiao, P. & Liu, Z. Microparticle image velocimetry (μ PIV) study of microcavity flow at low
364 Reynolds number. *Microfluid Nanofluidics* **19**, 403-417 (2015).
- 365 37. Shen, F., Xu, M., Wang, Z. & Liu, Z. Single-particle trapping, orbiting, and rotating in a microcavity using
366 microfluidics. *Appl Phys Express* **10**, 097301 (2017).
- 367 38. Shen, F., Xue, S., Xu, M., Pang, Y. & Liu Z. Experimental study of single-particle trapping mechanisms into
368 microcavities using microfluidics. *Phys Fluids* **31**, 042002 (2019).
- 369 39. Maxey, M.R. & Riley, J.J. Equation of motion for a small rigid sphere in a nonuniform flow. *Phys Fluids* **26**,
370 883-889 (1983).
- 371 40. Wereley, S.T. & Lueptow, R. M. Inertial particle motion in a Taylor Couette rotating filter. *Phys Fluids*, **11(2)**,
372 325-333 (1999).
- 373 41. Rallabandi, B. Inertial forces in the Maxey-Riley equation in nonuniform flows. *Phys Rev Fluids* **6**, L012302
374 (2021).
375

376 **Acknowledgements** This research was supported by the National Natural Science Foundation of China (Project No.
377 11872083), Project of Beijing Municipal Education Commission (Grant No. KZ201710005006) and Shandong Provincial
378 Natural Science Foundation (Project No. ZR2016AL07).

379 **Author Contributions** F.S. designed research; Z.H.L., S.X. and M.X. performed research; M.Z.A. and Z.M.L. analyzed
380 date; and F.S., M.Z.A. and Z.H.L. wrote the paper. All authors reviewed the final manuscript.

381 **Additional Information**

382 **Supplementary information** accompanies this paper at <https://doi.org/>

383 **Competing Interests:** The authors declare no competing interests.

Supplementary Files

This is a list of supplementary files associated with this preprint. Click to download.

- [MovieS1.mp4](#)
- [MovieS2.mp4](#)
- [MovieS3.mp4](#)
- [MovieS4.mp4](#)
- [MovieS5.mp4](#)
- [MovieS6.mp4](#)
- [MovieS7.mp4](#)
- [FigureS1.tif](#)
- [SRSupplementaryInformation.pdf](#)